Please cite this article as:

Rafael Piñol, Justyna Zeler, Carlos D. S. Brites, Yuanyu Gu, Pedro Téllez, Albano N. Carneiro Neto, Thiago E. da Silva, Raquel Moreno-Loshuertos, Patrício Fernandez-Silva, Ana Isabel Gallego, Luis Martinez-Lostao, Abelardo Martínez, Luís D. Carlos, and Angel Millán *Real-time intracellular temperature imaging using lanthanide-bearing polymeric micelles* **Nano Lett.** 2020, 20, 9, 6466–6472

Real-time intracellular temperature imaging using lanthanide-bearing polymeric micelles

Rafael Piñol[1], Justyna Zeler[2,3], Carlos D. S. Brites[2], Yuanyu Gu[1,4], Pedro Téllez[5], Albano N. Carneiro Neto[2], Thiago E. da Silva[2,6], Raquel Moreno-Loshuertos[7], Patricio Fernandez-Silva[7], Ana Gallego[7], Luis Martinez-Lostao[7], Abelardo Martínez[8], Luís D. Carlos[2*], Angel Millán[1*]

[1] ICMA, Institute of Materials Science of Aragon, CSIC-University of Zaragoza, 50008 Zaragoza, Spain
[2] Phantom-g, CICECO-Aveiro Institute of Materials, Department of Physics, University of Aveiro, Campus de Santiago, 3810-193 Aveiro, Portugal
[3] Faculty of Chemistry, University of Wroclaw, Wroclaw, Poland
[4] School of Materials Science and Engineering. Nanjing Tech University, 210009, Nanjing PR China
[5] Servicio de Apoyo a la Investigación. University of Zaragoza, C/ Pedro Cerbuna 10, 50006 Zaragoza, Spain
[6] Department of Fundamental Chemistry, Federal University of Pernambuco, 50670-901, Recife, PE, Brazil.
[7] Departamento de Bioquímica, Biología Molecular y Celular, Universidad de Zaragoza, Zaragoza, Spain
[8] Departamento de Electrónica de Potencia, I3A, Universidad de Zaragoza 50018 Zaragoza, Spain

Measurement of thermogenesis in individual cells is a remarkable challenge due to the complexity of the biochemical environment (such as pH and ionic strength) and to the rapid and yet not well-understood heat transfer mechanisms throughout the cell. Here, we present a unique system for intracellular temperature mapping in a fluorescence microscope (uncertainty of 0.2 K) using rationally designed luminescent Ln^{3+}-bearing polymeric micellar probes (Ln=Sm, Eu) incubated in breast cancer MDA-MB468 cells. 2D thermal images recorded increasing the temperature of the cells culture medium between 296 and 304 K shows inhomogeneous intracellular temperature progressions up to ~20 degrees and subcellular gradients of ~5 degrees between the nucleolus and the rest of the cell, illustrating the thermogenic activity of the different organelles and highlighting the potential of this tool to study intracellular processes.

Keywords: Intracellular temperature mapping, Luminescence thermometry, Thermogenesis, Lanthanide-based polymer nanomicelles

Temperature affects everything and temperature fluctuations play a central role in the myriad of biochemical reactions regulating life.[1] The intracellular temperature, for instance, changes with cellular activity, including cell division, gene expression, enzymatic reactions, and pathological states.[2-4] Moreover, to neutralize large external temperature changes and to keep homeostasis of the body temperature upon cold or hot exposure, cells have developed thermoregulation mechanisms.[3-7] Despite recognition of the fundamental involvement of temperature in eliciting biochemical changes,[8-10] specific molecular mechanisms by which cells produce and use heat are largely unknown,[4, 7, 11-18], which, thus, have driven the research on intracellular thermometers in the past decade. Although there are a handful of reported intrusive intracellular thermometers,[6, 19, 20] contactless luminescence-based examples have been largely the most adopted strategy.[9, 10, 21-27] Indeed, several types of luminescent materials have been proposed for intracellular temperature sensing such as organic molecules,[21, 28, 29] polymers,[30, 31] carbon dots,[32] quantum dots,[33] N-vacancy nanodiamonds,[2] and trivalent lanthanide ions (Ln^{3+})-doped inorganic nanoparticles[34] and organic-inorganic hybrids.[35]

These luminescent thermometers unveiled intriguing spatiotemporal intracellular temperature fluctuations, including organelle-specific thermogenesis, suggesting a fundamental connection between the temperature and the cell functions.[4, 7-10] For example, Chrétien *et al.*[17] correlated changes in the mitochondrial temperature with the oxygen consumption, showing that the mitochondrial temperature is up to 10 degrees higher than the body temperature when the respiratory chain was fully functional. Also, Tanimoto *et al.*[36] observed temperature differences up to 6 degrees in micrometer scale domains in a neuronal cell after the mitochondrial stimulation, whereas Rajagopal *et al*.[6] reported temperature spikes of ~7.5 degrees during stimulated proton uncoupling in neurons of *Aplysia californica*. Finally, Yang *et al*.[33] and Liu *et al*.[37] showed inhomogeneous intracellular temperature distributions up to 10–15 degrees

higher than the temperature of the living cells culture medium, following, respectively, Ca^{2+} stress and cold shock, and externally-induced temperature changes. All these observations (among other examples[5, 30]) are inconsistent with theoretical calculations suggesting that maximal heat gradients across cells could not be greater than 10^{-5} K.[7, 11, 16, 18]

Here, we report intriguing real-time bidimensional (2D) temperature maps of breast metastatic adenocarcinoma cells (line MDA-MB-468) incubated with innovative Ln^{3+}-bearing polymeric micelles. The thermal images show inhomogeneous intracellular temperature progressions up to ~20 degrees and subcellular temperature gradients of ~5 degrees raising the exciting possibility of using these gradients for signaling and regulation in cells,[33] and emphasizing the present misunderstood about the response of living cells to temperature variations.

A scheme of the synthesis of the micelles is presented in Figure 1. It consists of a self-organized structure formed using a single polymer containing hydrophilic and hydrophobic blocks. The amphiphilic block is the P(MPEGA-co-PEGA)-b-P(MA-b-PhenA) copolymer (MPEGA and PEGA stand for poly(ethylene glycol) methyl ether acrylate and polyethyleneglycol acrylate, respectively) and was synthesized by reversible addition-fragmentation chain transfer polymerization (details in the Supporting Information). The hydrophobic block is a methyl acrylate (MA) polymer containing a discrete number of the auxiliary ligand 4-(acryloyloxymethyl)-1,10-phenanthroline (PhenA) to complete the coordination sphere of the Ln^{3+} ion and shield the complex from the influence of the medium by steric effects. We rationally design the polymeric micelles and the Ln^{3+} complexes to mitigate luminescence quenching effects induced by the culture medium and the proposed copolymerization strategy permits easy incorporation of other functionalities such as tags for different cell organelles. The hydrodynamic diameter of the resulting micelles in aqueous suspension gives a monomodal distribution with an average diameter of 20.3±0.2 nm (Figure 1b,c). The scanning transmission electron micrographs showed particles, with

a granular texture and bright spots (discernible at high magnification), which is compatible with the presence of Ln^{3+} complexes within the micelle. Moreover, the electron dispersive scattering (EDS) within the micelles presents the signature of Sm, whereas less frequent Eu, was only faintly detected (Figure S2 in Supporting Information). These elements were not observed outside the micelles.

The photoluminescence studies on the Ln^{3+}-bearing polymeric micelles are summarized in Figure 2. A remarkable excitation peak at 436 nm, in the blue-violet spectral range, is discerned (Figure 2a). This is an important achievement because contrary to other thermometric systems that need high-energetic (and cell harmful) ultraviolet excitation, using excitation in the visible spectral range circumvents damage to the cultured cells under observation, and it can be easily used in conventional confocal microscopes and that do not natively incorporate UV laser sources.

The thermal dependence of the emission spectra was recorded in the 300–328 K range for the aqueous suspension of the Eu^{3+}- and Sm^{3+}-bearing polymeric micelles (Figure 2b-d). In the case of btfa-based micelles, the integrated area of the Sm^{3+} $^4G_{5/2}\rightarrow{}^6H_{9/2}$ transition (I_1) decreases with increasing temperature by ~12%, that of the Eu^{3+}, $^5D_0\rightarrow{}^7F_2$ transition (I_2) is reduced by 40% of the initial value (Figure 3a). According to the DNPD-based material, the temperature-dependent trend is more evident. The emission of Eu^{3+} decreases increasing temperature (leaving ~18% of the RT intensity), and what is more also the emission of Sm^{3+} is reduced ~4 times at the highest temperature (Figure 3b). To rationalize these thermal dependences, we use time-dependent density functional theory and intramolecular energy transfer calculations (details in Supporting Information). The intramolecular energy transfer rates for Ln^{3+} complexes were estimated based on a well-defined theory.[38-42]

The main energy-transfer pathways in the micelles containing the DNPD complexes (Figure 3c) involves the $T_1\rightarrow{}^5D_0$ (Eu^{3+}) and $T_1\rightarrow{}^4G_{5/2}$ (Sm^{3+}) transitions corresponding respectively to ~83% and ~91% of the total forward intramolecular energy transfer rates. On one hand, the backward energy transfer rates (W_{bET})

increase at temperature increase, depopulating the $^5D_0$ (Eu^{3+}) and $^4G_{5/2}$ (Sm^{3+}) emitting levels and, on the other hand, W_{bET} for Eu^{3+} is more affected by the temperature increase than those of Sm^{3+}. The balance between these two processes explains the stepper decay observed for the integrated area of $^5D_0 \rightarrow {}^7F_2$ transition in comparison with that of $^4G_{5/2} \rightarrow {}^6H_{9/2}$ (Figure 3b). In the btfa-Ln^{3+} complexes, the T_1 state (15480 cm^{-1}) is lying below the Eu^{3+} and Sm^{3+} ion acceptor states, leading to a higher energy barrier. Consequently, the energy transfer pathways involving the S_1 state (34300 cm^{-1}) as donor become more operative (in order of 10^4 and 10^6 s^{-1}, respectively, Tables S5 and S6). According to the simulations, the energy transfer from the S_1 represents 93.4% and 93.8% of the total for Eu^{3+} and Sm^{3+} ions, respectively. For the btfa ligand, the energy transfer involves the non-radiative decays from the lanthanides' higher energy states to the corresponding emitting levels. Since the population of the emitting levels is dependent on its decay lifetimes (that are in order of 10^{-3} s), it has time enough to transfer energy to the triplet state (in order of 10^4 s^{-1} for Eu^{3+} and 10^5 s^{-1} for Sm^{3+}). This means that the population of the emitting level is dependent on the balance between the population increase resulting from the singlet (W_{Ln}^{S}) and the population decrease due to lanthanide-to-btfa triplet state ($W_{T_1}^{Ln}$) energy transfers, which allow us to define an effective transition rate as $W^* = W_{Ln}^{S} - W_{T_1}^{Ln}$. Figure S7 presents the temperature dependence of the normalized W^*. The rate for the $Eu^{3+} \rightarrow T_1$ energy transfer is of the same order of magnitude of that of $S_1 \rightarrow Eu^{3+}$ in the higher energetic states. In contrast, for the btfa-Sm^{3+} complex, the $W_{T_1}^{Ln}$ is one order of magnitude lower than the W_{Ln}^{S}, explaining the lower temperature quenching of the Sm^{3+} integrated area in comparison with the Eu^{3+} one presented in Figure 3a.

The integrated areas of the $^4G_{5/2} \rightarrow {}^6H_{9/2}$ (I_1, Sm^{3+}) and $^5D_0 \rightarrow {}^7F_2$ (I_2, Eu^{3+}) transitions are used to define the thermometric parameter $\Delta = I_2/I_1$. The $\Delta(T)$ dependence is well fitted by empirical polynomial equations for both ligands (Figure S9 in Supporting Information). The relative thermal sensitivity (Figure S10 in Supporting Information) of

the micelles increases with the temperature increase reaching the maximum value of 1.5 %. K^{-1} and 1.7 %. K^{-1} for btfa- and DNPD-containing micelles, respectively, both at 328 K. The minimum temperature uncertainty is remarkably low, 6 mK (at 328 K), and 0.20 K (at 305 K) for the btfa- and DNPD-containing micelles (Figure S12 in Supporting Information). Whereas the relative thermal sensitivity values are lower than that reported for similar micelles containing Tb^{3+} ions[35] (5.8 %·K^{-1} at 296 K), the decrease of the relative uncertainty on the integrated intensity to unprecedented values of $\delta I/I<0.4\%$ (Figure S11 in Supporting Information) allowed us to design the first luminescent thermometer with temperature uncertainty values below 10 mK.

These exciting results of thermometric performance motivate the development of a temperature-imaging instrument (Figure S3 in Supporting Information). It consists of a fluorescence microscope that incorporates a beam splitter, a CMOS camera, and a CCD camera. The illumination light is filtered through a 340–380 nm bandpass filter and reflected with a 400 nm dichroic mirror. The emission beam is divided into two by a 635 nm dichroic mirror and the resulting beams are filtered through the 600−620 nm and 620–660 nm bandpass filters that roughly cover the $^5D_0 \rightarrow {}^7F_2$ (Eu^{3+}) and $^4G_{5/2} \rightarrow {}^6H_{9/2}$ (Sm^{3+}) emissions. Finally, both the Eu^{3+} and Sm^{3+} filtered beams are collected by a'' CMOS camera (Figure S3b in Supporting Information). All the process of temperature imaging is controlled by a LabView image-processing sequence. A MatLab® routine (developed by us) is then used to process the original CMOS image containing both the $Eu^{3+}$and Sm^{3+} emission to get 2D temperature maps (Figure S3b in Supporting Information). The temperature-mapping routine first separates the original image into the corresponding Sm^{3+} (I_1) and Eu^{3+} (I_2) emissions. Then, the intensity values for the equivalent pixels of Eu^{3+} and Sm^{3+} images are identified, and the intensity ratio $\Delta=I_2/I_1$ is calculated and converted into temperature by the corresponding calibration curve. Finally, we obtain a 2D temperature matrix that is represented as a false-color image that can be overlapped to the original image, mapping the temperature distribution of the cellular culture.

Despite both the btfa- and DNPD-based Ln^{3+}-bearing polymeric micelles are stable in water, in the presence of the culture medium the btfa-based polymeric micelles present a poor emission intensity in the same excitation conditions of DNPD-based ones (Figure S16 in Supporting Information). The time-dependent density functional theory and the intramolecular energy transfer calculations point out that the btfa-based micelles undergo a luminescence quenching process due to the energy transfer that involves the Ln^{3+} emitting levels to the T_1 state. On the contrary, in the DNPD-based micelles is the balance between the S_1-to-Ln^{3+} and the Ln^{3+}-to-T_1 energy transfers that rules the temperature dependence of the intensities (details *in silico* experiments in Supporting Information).

In a proof-of-concept experiment, the thermometric imaging system was tested with MDA-MB-468 breast cancer cells incubated with DNPD-based polymeric micelles. The cells were observed before and after incubation with the Ln^{3+}-bearing polymeric micelles (culture details in Supporting Information). Phase-contrast images (Figure 4a,b) showed that the cells were well-formed and uniformly spread. Grayscale images showed the luminescence of internalized Ln^{3+}-bearing polymeric micelles in both the Sm^{3+} and the Eu^{3+} channels (Figure 4c,d, and Figure S16c,d in Supporting Information), whereas images from control cells before incubation with the micelles were totally dark (Figure S14 in Supporting Information). These results are compatible with the cell internalization of the Ln^{3+}-bearing polymeric micelles and indicate their stability on cellular medium. Moreover, the mean temperature determined in both the fixed and live cells agree very well with the temperature values of the cellular culture (298.0 and 296.5 K, respectively, Figures S16 and S17 in Supporting Information). Interestingly, the temperature distribution is much narrower in the fixed cells (standard error of 0.02 K, Figure S16 in Supporting Information) than in the live cell (standard error >0.5 K Figure S17 in Supporting Information).

The phase-contrast images of the cell cultures incubated with DNPD-based polymeric micelles display brighter regions under UV-light illumination (yellow arrows in

Figure 4c,d) corresponding to areas of higher accumulation of the luminescent probes. Although the detailed analysis of the distribution of the nanoparticles within the cell lies out of the scope of the present work, and the identification of the spherical brighter areas would require the use of biological markers, from a morphological point of view these spots might correspond to the cells' nucleolus. To evaluate the effect of an external heat source in the temperature distribution at subcellular regions, we use a temperature controller attached to the imaging instrument described above. A total of 450 points were sampled (150 in the brighter and 300 in the darker regions) within the limits of 3 MDA-MB-468 cells for each temperature set between 296.45 and 303.55 K (Figure 5a-d). The histograms of both dark and bright regions display an inhomogeneous intracellular temperature progression up to ~20 degrees (Figure 5e-h), which is consistent with the previous reports on temperature mappings on living cells using diverse fluorophores as temperature probes[17, 33, 36, 37] (Table S8). Furthermore, all the histograms follow Gaussian distributions centered at values that increase with the external temperature set in the controller (Figure 5e-i). Remarkably, whereas for the darker regions the average temperatures are in excellent agreement with those set externally, for the brighter areas we observe an average temperature ~5 degrees higher than that of the rest of the cell (Figure 5i). This temperature increment is of the same order of magnitude than that already observed by Okabe *et al.*[30] and could be explained by the intense RNA transcription activity of the nucleolus.[43, 44]

In summary, we reported here a unique system for real-time intracellular temperature mapping of living cells based on innovative luminescent Eu^{3+}/Sm^{3+}-bearing polymeric micellar probes. The micelles and the Ln^{3+} complexes covalently bonded to its hydrophobic part were rationally designed to mitigate quenching effects induced by the culture medium. Moreover, the copolymerization strategy proposed permits easy incorporation of other functionalities, such as targeting different cell organelles, and the temperature is recorded from the ratio between the integrated areas of the $^4G_{5/2} \rightarrow {}^6H_{9/2}$ and $^5D_0 \rightarrow {}^7F_2$ transitions of the Sm^{3+} and Eu^{3+} ions,

respectively, using a conventional (or minimally adapted) fluorescence microscope. A proof-of-concept experiment on breast metastatic adenocarcinoma cells (line MDA-MB-468) incubated with the Eu^{3+}/Sm^{3+}-bearing micelles under UV-light excitation yields 2D thermal images in the 296–304 K range with an uncertainty of 0.2 K. The thermal images allow us to delimitate the cells and to identify its nucleolus as brighter regions. By increasing the temperature of the culture medium, inhomogeneous intracellular temperature progressions up to ~20 degrees and an increment of ~5 degrees of the nucleolus temperature relative to the rest of the cell were discerned, which might be related to the activity of the thermo-generating organelles and highly exoenergetic processes. The real-time intracellular temperature imaging using these Ln^{3+}-bearing polymeric micelles opens new avenues to the detailed screening of thermal gradients within living cells due to endogenous or exogenous stimuli, providing important insights into the regulatory intracellular mechanisms, and thus contributing to an improved comprehension of the role of some subcellular thermo-generating organelles in the cellular functions.

Associated Content

Supporting Information: Materials and methods, Thermometric-imaging system, *In silico* experiments, Photoluminescence, Thermometric performance of the Ln^{3+}-bearing micelles, Cell cultures, and Temperature imaging.

Author Information

Corresponding Authors
Luís D. Carlos
e-mail: lcarlos@ua.pt

Angel Millán
e-mail: amillan@unizar.es

Author Contributions
The manuscript was written through the contributions of all authors. RP synthetized the thermometric micelles, JZ recorded the photoluminescent measurements; CDSB wrote the MatLab routines, analyzed the microscopy images and the photoluminescent results, and draw the figures; YG performed the microscopy observations, ANCN and TES performed the in-silico experiments; PT and AM developed the cell temperature imaging experimental set-up; RM, PFS, AG, and LML performed the cell culture

experiments; LDC and AM wrote the paper and co-supervised the project. All authors have approved the final version of the manuscript.

Acknowledgments

This work was developed within the scope of the project CICECO-Aveiro Institute of Materials, UIDB/50011/2020 & UIDP/50011/2020, financed by Portuguese funds through the FCT/MEC and when appropriate co-financed by FEDER under the PT2020 Partnership Agreement. Financial support from the project (NanoHeatControl, POCI-01-0145-FEDER-031469), funded by FEDER, through POCI and by Portuguese funds (OE), through FCT/MCTES, by European Union's Horizon 2020 FET Open program under grant agreements no. 801305 and 829162, Spanish Ministry of Science Innovation and Universities (Grant No: PGC2018_095795_B_I00) and Diputación General de Aragón (E11/17R) are acknowledged. ANCN thanks SusPhotoSolutions project, CENTRO-01-0145-FEDER-000005, Portugal for his grant. The authors acknowledge the use of Servicio General de Apoyo a la Investigación-SAI, Universidad de Zaragoza.

Abbreviations

btfa - 4,4,4-trifluoro-1-phenyl-1,3-butanedione; DNPD - 1,3-di(naphthalen-2-yl)propane-1,3-dione; MPEGA - methoxy polyethylene glycol acrylate; PEGA - polyethylene glycol acrylate; MA - methyl acrylate; PhenA - 1,10-phenanthrolin-4-yl)methyl acrylate.

References

1. Precht, H. *Temperature and Life*; Springer Science & Business Media: Berlin, 2013.
2. Kucsko, G.; Maurer, P. C.; Yao, N. Y.; Kubo, M.; Noh, H. J.; Lo, P. K.; Park, H.; Lukin, M. D. Nanometre-Scale Thermometry in a Living Cell. *Nature* **2013,** *500* (7460), 54-58, DOI: 10.1038/Nature12373.
3. Ibraimov, A. I. Cell Thermoregulation: Problems, Advances and Perspectives. *J. Mol. Biol. Res.* **2017,** *7* (1), 58-79, DOI: 10.5539/jmbr.v7n1p58.
4. Okabe, K.; Sakaguchi, R.; Shi, B.; Kiyonaka, S. Intracellular Thermometry with Fluorescent Sensors for Thermal Biology. *Pflug. Arch. Eur. J. Phy.* **2018,** *470* (5), 717-731, DOI: 10.1007/s00424-018-2113-4.
5. Kiyonaka, S.; Kajimoto, T.; Sakaguchi, R.; Shinmi, D.; Omatsu-Kanbe, M.; Matsuura, H.; Imamura, H.; Yoshizaki, T.; Hamachi, I.; Morii, T.; Mori, Y. Genetically Encoded Fluorescent Thermosensors Visualize Subcellular Thermoregulation in Living Cells. *Nat. Methods* **2013,** *10* (12), 1232-1238, DOI: 10.1038/Nmeth.2690.
6. Rajagopal, M. C.; Brown, J. W.; Gelda, D.; Valavala, K. V.; Wang, H.; Llano, D. A.; Gillette, R.; Sinha, S. Transient Heat Release During Induced Mitochondrial Proton Uncoupling. *Commun. Biol.* **2019,** *2*, DOI: 10.1038/s42003-019-0535-y.
7. Suzuki, M.; Plakhotnik, T. The Challenge of Intracellular Temperature. *Biophys. Rev.* **2020**, DOI: 10.1007/s12551-020-00683-8.
8. Takei, Y.; Arai, S.; Murata, A.; Takabayashi, M.; Oyama, K.; Ishiwata, S.; Takeoka, S.; Suzuki, M. A Nanoparticle-Based Ratiometric and Self-Calibrated Fluorescent Thermometer for Single Living Cells. *ACS Nano* **2014,** *8* (1), 198-206, DOI: 10.1021/Nn405456e.
9. Bai, T. T.; Gu, N. Micro/Nanoscale Thermometry for Cellular Thermal Sensing. *Small* **2016,** *12* (34), 4590-4610, DOI: 10.1002/smll.201600665.
10. Uchiyama, S.; Gota, C.; Tsuji, T.; Inada, N. Intracellular Temperature Measurements with Fluorescent Polymeric Thermometers. *Chem. Commun.* **2017,** *53* (80), 10976-10992, DOI: 10.1039/c7cc06203f.
11. Baffou, G.; Rigneault, H.; Marguet, D.; Jullien, L. A Critique of Methods for Temperature Imaging in Single Cells. *Nat. Methods* **2014,** *11* (9), 899-901, DOI: 10.1038/nmeth.3073.
12. Arai, S.; Lee, S.-C.; Zhai, D.; Suzuki, M.; Chang, Y. T. A Molecular Fluorescent Probe for Targeted Visualization of Temperature at the Endoplasmic Reticulum. *Sci. Rep.-UK* **2014,** *4*, DOI: 10.1038/srep06701.
13. Kiyonaka, S.; Sakaguchi, R.; Hamachi, I.; Morii, T.; Yoshizaki, T.; Mori, Y. Validating Subcellular Thermal Changes Revealed by Fluorescent Thermosensors. *Nat. Methods* **2015,** *12* (9), 801-802, DOI: 10.1038/nmeth.3548.
14. Baffou, G.; Rigneault, H.; Marguet, D.; Jullien, L. "Validating Subcellular Thermal Changes Revealed by Fluorescent Thermosensors" and "the 10(5) Gap Issue between Calculation and Measurement in Single-Cell Thermometry" Reply. *Nat Methods* **2015,** *12* (9), 803-803, DOI :10.1038/nmeth.3552.
15. Suzuki, M.; Zeeb, V.; Arai, S.; Oyama, K.; Ishiwata, S. The 10^5 Gap Issue between Calculation and Measurement in Single-Cell Thermometry. *Nat. Methods* **2015,** *12* (9), 802-803, DOI: 10.1038/nmeth.3551.
16. Kriszt, R.; Arai, S.; Itoh, H.; Lee, M. H.; Goralczyk, A. G.; Ang, X. M.; Cypess, A. M.; White, A. P.; Shamsi, F.; Xue, R. D.; Lee, J. Y.; Lee, S. C.; Hou, Y. Y.; Kitaguchi, T.; Sudhaharan, T.; Ishiwata, S.; Lane, E. B.; Chang, Y. T.; Tseng, Y. H.; Suzuki, M.; Raghunath, M. Optical Visualisation of Thermogenesis in Stimulated Single-Cell Brown Adipocytes. *Sci. Rep.-UK* **2017,** *7*, 1383, DOI: 10.1038/s41598-017-00291-9.
17. Chrétien, D.; Bénit, P.; Ha, H. H.; Keipert, S.; El-Khoury, R.; Chang, Y. T.; Jastroch, M.; Jacobs, H. T.; Rustin, P.; Rak, M. Mitochondria Are Physiologically

Maintained at Close to 50 Degrees C. *PLOS Biol.* **2018,** *16* (1), e2003992, DOI: 10.1371/journal.pbio.2003992.
18. Lane, N. Hot Mitochondria? *PLOS Biol.* **2018,** *16* (1), e2005113, DOI: 10.1371/journal.pbio.2005113.
19. Suzuki, M.; Tseeb, V.; Oyama, K.; Ishiwata, S. Microscopic Detection of Thermogenesis in a Single Hela Cell. *Biophys. J.* **2007,** *92* (6), L46-L48, DOI 10.1529/biophysj.106.098673.
20. Yang, F.; Li, G.; Yang, J. M.; Wang, Z. H.; Han, D. H.; Zheng, F. J.; Xu, S. Y. Measurement of Local Temperature Increments Induced by Cultured Hepg2 Cells with Micro-Thermocouples in a Thermally Stabilized System. *Sci Rep-Uk* **2017,** *7*, DOI: 10.1038/s41598-017-01891-1.
21. Huang, H.; Delikanli, S.; Zeng, H.; Ferkey, D. M.; Pralle, A. Remote Control of Ion Channels and Neurons through Magnetic-Field Heating of Nanoparticles. *Nat. Nanotechnol.* **2010,** *5* (8), 602-606, DOI: 10.1038/Nnano.2010.125.
22. Jaque, D.; del Rosal, B.; Rodríguez, E. M.; Maestro, L. M.; Haro-González, P.; Solé, J. G. Fluorescent Nanothermometers for Intracellular Thermal Sensing. *Nanomedicine* **2014,** *9* (7), 1047-1062, DOI: 10.2217/Nnm.14.59.
23. Sakaguchi, R.; Kiyonaka, S.; Mori, Y. Fluorescent Sensors Reveal Subcellular Thermal Changes. *Curr. Opin. Biotech.* **2015,** *31*, 57-64, DOI: 10.1016/j.copbio.2014.07.013.
24. Carlos, L. D.; Palacio, F. *Thermometry at the Nanoscale: Techniques and Selected Applications*; Royal Society of Chemistry: Oxfordshire, 2016.
25. Quintanilla, M.; Liz-Marzan, L. M. Guiding Rules for Selecting a Nanothermometer. *Nano Today* **2018,** *19*, 126-145, DOI: 10.1016/j.nantod.2018.02.012.
26. Brites, C. D. S.; Balabhadra, S.; Carlos, L. D. Lanthanide-Based Thermometers: At the Cutting-Edge of Luminescence Thermometry. *Adv. Opt. Mater.* **2019,** *7* (5), 1801239, DOI: 10.1002/adom.201801239.
27. Nakano, M.; Nagai, T. Thermometers for Monitoring Cellular Temperature. *J. Photoch. Photobio. C* **2017,** *30*, 2-9, DOI: 10.1016/j.jphotochemrev.2016.12.001.
28. Freddi, S.; Sironi, L.; D'Antuono, R.; Morone, D.; Dona, A.; Cabrini, E.; D'Alfonso, L.; Collini, M.; Pallavicini, P.; Baldi, G.; Maggioni, D.; Chirico, G. A Molecular Thermometer for Nanoparticles for Optical Hyperthermia. *Nano Lett.* **2013,** *13* (5), 2004-2010, DOI: 10.1021/Nl400129v.
29. Savchuk, O. A.; Silvestre, O. F.; Adão, R. M. R.; Nieder, J. B. Gfp Fluorescence Peak Fraction Analysis Based Nanothermometer for the Assessment of Exothermal Mitochondria Activity in Live Cells. *Sci. Rep.-UK* **2019,** *9*, 7535, DOI: 10.1038/s41598-019-44023-7.
30. Okabe, K.; Inada, N.; Gota, C.; Harada, Y.; Funatsu, T.; Uchiyama, S. Intracellular Temperature Mapping with a Fluorescent Polymeric Thermometer and Fluorescence Lifetime Imaging Microscopy. *Nat. Commun.* **2012,** *3*, 705, DOI: 10.1038/ncomms1714.
31. Inada, N.; Fukuda, N.; Hayashi, T.; Uchiyama, S. Temperature Imaging Using a Cationic Linear Fluorescent Polymeric Thermometer and Fluorescence Lifetime Imaging Microscopy. *Nat. Protoc.* **2019,** *14* (4), 1293-1321, DOI: 10.1038/s41596-019-0145-7.
32. Kalytchuk, S.; Polakova, K.; Wang, Y.; Froning, J. P.; Cepe, K.; Rogach, A. L.; Zboril, R. Carbon Dot Nanothermometry: Intracellular Photoluminescence Lifetime Thermal Sensing. *ACS Nano* **2017,** *11* (2), 1432-1442, DOI: 10.1021/acsnano.6b06670.
33. Yang, J. M.; Yang, H.; Lin, L. W. Quantum Dot Nano Thermometers Reveal Heterogeneous Local Thermogenesis in Living Cells. *ACS Nano* **2011,** *5* (6), 5067-5071, DOI: 10.1021/Nn201142f.
34. Vetrone, F.; Naccache, R.; Zamarron, A.; de la Fuente, Á. J.; Sanz-Rodríguez, F.; Maestro, L. M.; Rodríguez, E. M.; Jaque, D.; Solé, J. G.; Capobianco, J. A.

Temperature Sensing Using Fluorescent Nanothermometers. *ACS Nano* **2010,** *4* (6), 3254-3258, DOI: 10.1021/Nn100244a.

35. Piñol, R.; Brites, C. D. S.; Bustamante, R.; Martínez, A.; Silva, N. J. O.; Murillo, J. L.; Cases, R.; Carrey, J.; Estepa, C.; Sosa, C.; Palacio, F.; Carlos, L. D.; Millán, A. Joining Time-Resolved Thermometry and Magnetic-Induced Heating in a Single Nanoparticle Unveils Intriguing Thermal Properties. *ACS Nano* **2015,** *9* (3), 3134-3142, DOI: 10.1021/acsnano.5b00059.
36. Tanimoto, R.; Hiraiwa, T.; Nakai, Y.; Shindo, Y.; Oka, K.; Hiroi, N.; Funahashi, A. Detection of Temperature Difference in Neuronal Cells. *Sci. Rep.-UK* **2016,** *6*, 22071, DOI: 10.1038/srep22071.
37. Liu, H. L.; Fan, Y. Y.; Wang, J. H.; Song, Z. S.; Shi, H.; Han, R. C.; Sha, Y. L.; Jiang, Y. Q. Intracellular Temperature Sensing: An Ultra-Bright Luminescent Nanothermometer with Non-Sensitivity to Ph and Ionic Strength. *Sci. Rep-.UK* **2015,** *5*, 14879, DOI: 10.1038/srep14879.
38. Malta, O. L. Ligand-Rare-Earth Ion Energy Transfer in Coordination Compounds. A Theoretical Approach. *J. Lumin.* **1997,** *71* (3), 229-236,
39. Silva, F. R. G. E.; Malta, O. L. Calculation of the Ligand-Lanthanide Ion Energy Transfer Rate in Coordination Compounds: Contributions of Exchange Interactions. *J. Alloy. Compd.* **1997,** *250* (1-2), 427-430, DOI: 10.1016/S0925-8388(96)02563-7.
40. Malta, O. L.; Silva, F. R. G. E. A Theoretical Approach to Intramolecular Energy Transfer and Emission Quantum Yields in Coordination Compounds of Rare Earth Ions. *Spectrochim. Acta A* **1998,** *54* (11), 1593-1599,
41. Malta, O. L. Mechanisms of Non-Radiative Energy Transfer Involving Lanthanide Ions Revisited. *J. Non-Cryst. Solids* **2008,** *354* (42-44), 4770-4776, DOI 10.1016/j.jnoncrysol.2008.04.023.
42. Carneiro Neto, A. N.; Teotonio, E. E. S.; de Sá, G. F.; Brito, H. F.; Legendziewicz, J.; Carlos, L. D.; Felinto, M. C. F. C.; Gawryszewska, P.; Moura, R. T.; Longo, R. L.; Faustino, W. M.; Malta, O. L., Modeling Intramolecular Energy Transfer in Lanthanide Chelates: A Critical Review and Recent Advances. In *Handbook on the Physics and Chemistry of Rare Earths*, Bünzli, J.-C. G.; Pecharsky, V. K., Eds. Elsevier: 2019; Vol. 56, pp 55-162.
43. Berry, J.; Weber, S. C.; Vaidya, N.; Haataja, M.; Brangwynne, C. P. Rna Transcription Modulates Phase Transition-Driven Nuclear Body Assembly. *P. Natl. Acad. Sci. USA* **2015,** *112* (38), E5237-E5245, DOI: 10.1073/pnas.1509317112.
44. Boisvert, F. M.; van Koningsbruggen, S.; Navascues, J.; Lamond, A. I. The Multifunctional Nucleolus. *Nat. Rev. Mol. Cell. Bio.* **2007,** *8* (7), 574-585, DOI: 10.1038/nrm2184.

Figures

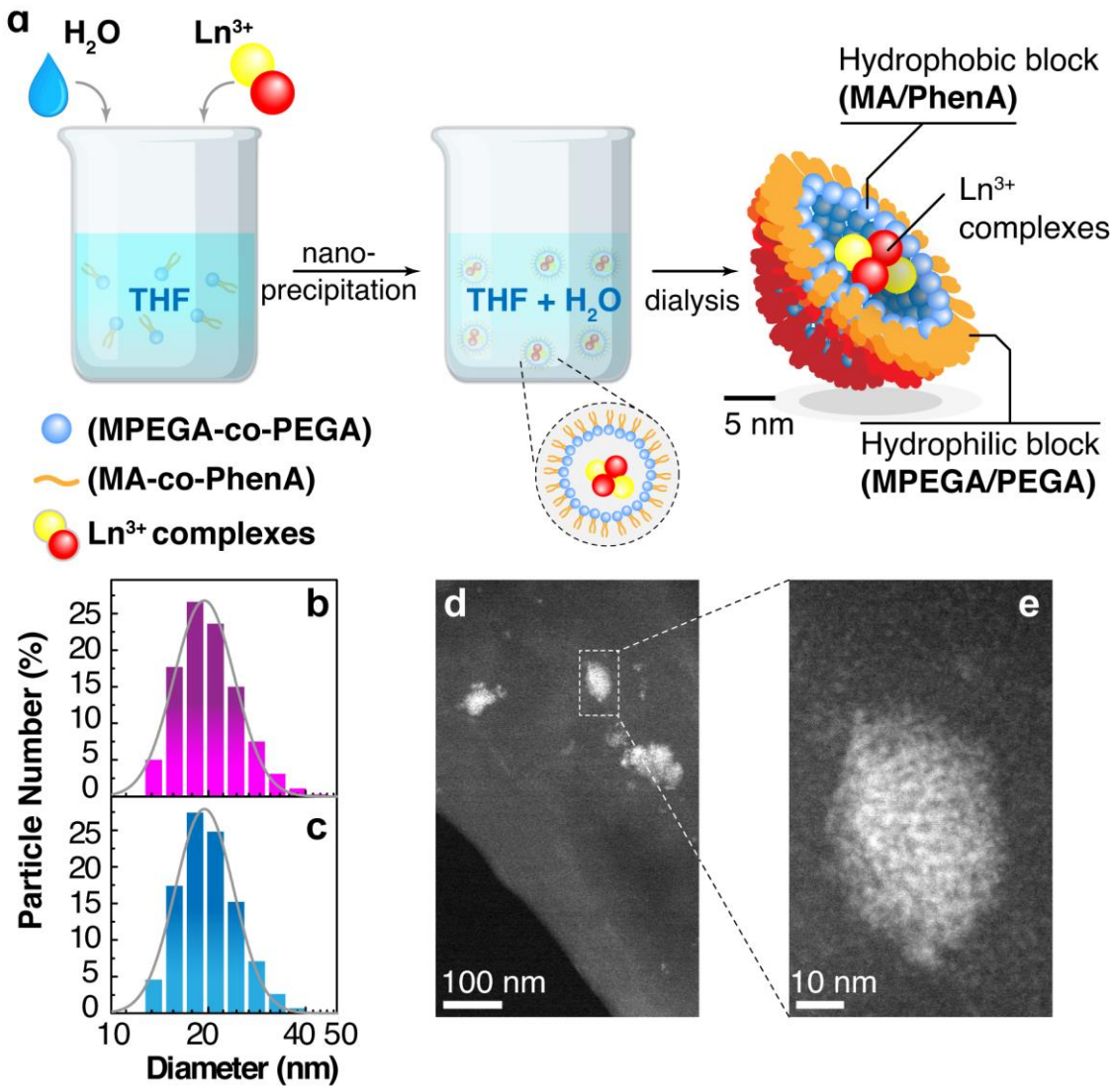

Figure 1. (a) Flux diagram of the synthesis route used to produce the Ln^{3+}-bearing polymeric micelles. Dynamic light scattering size distribution of the Ln^{3+}-bearing **(b)** btfa- and **(c)** DNPD- based polymeric micelles after filtration through a 100 nm membrane filter. The solid lines are the best fit to log-normal distributions (r^2>0.99) centered at 20.3±0.2 nm in both cases. **(d,e)** Scanning transmission electron microscope images of the Ln^{3+}-bearing btfa-based polymeric micelles.

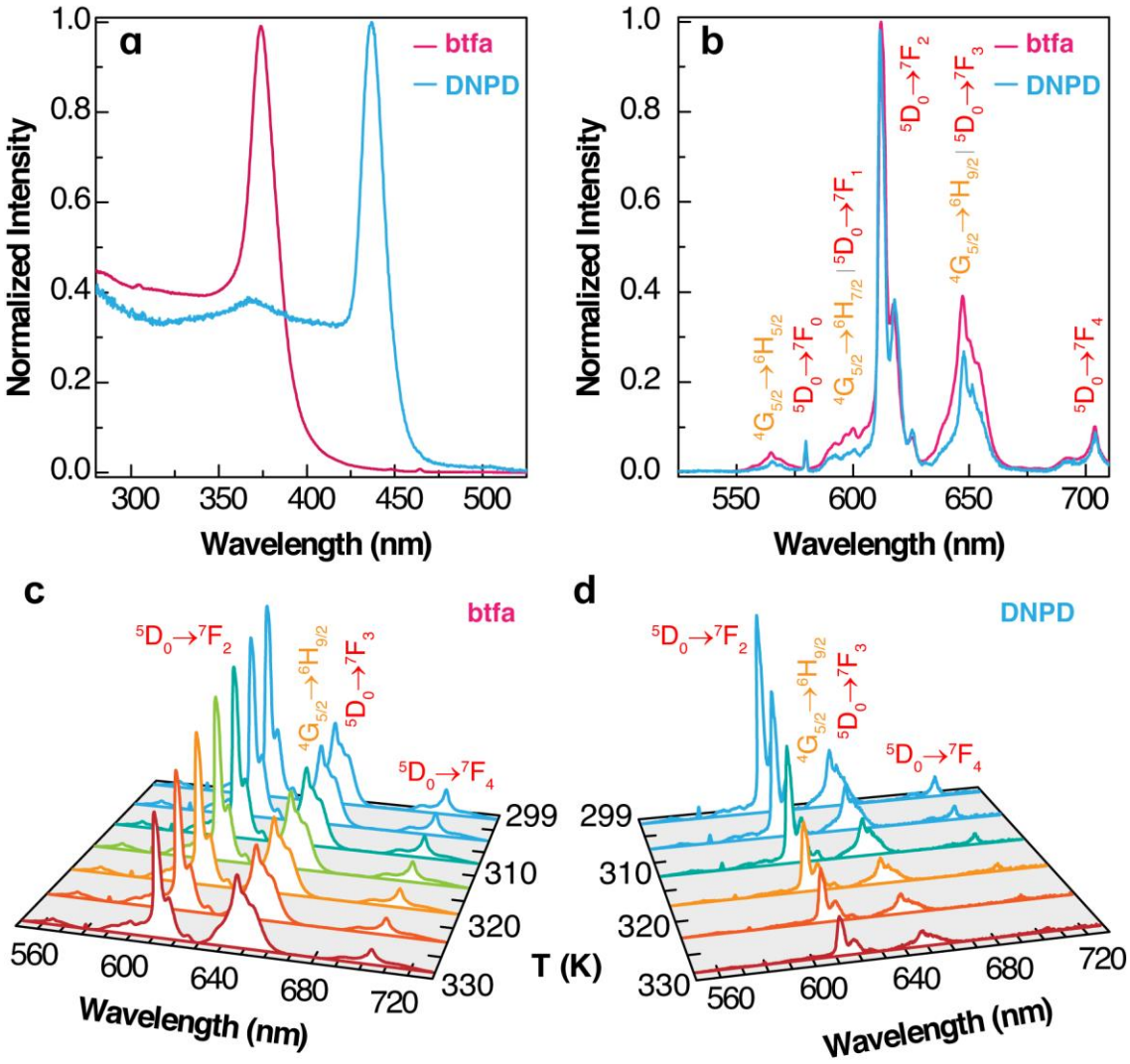

Figure 2. (a) Excitation spectra of btfa- and DNPD-based polymeric micelles at room temperature monitoring the $^5D_0 \rightarrow {}^7F_2$ transition of Eu^{3+}. **(b)** Room temperature emission spectra of the btfa- and DNPD-based polymeric micelles. The transitions ascribed to Eu^{3+} and Sm^{3+} are signed in red and orange, respectively. Temperature dependence of the emission spectra recorded in the 299–328 K range for **(c)** btfa- and **(d)** DNPD-based polymeric micelles. In (b), (c) and (d) the excitation wavelengths used are 373 nm and 436 nm for btfa- and DNPD-based micelles, respectively.

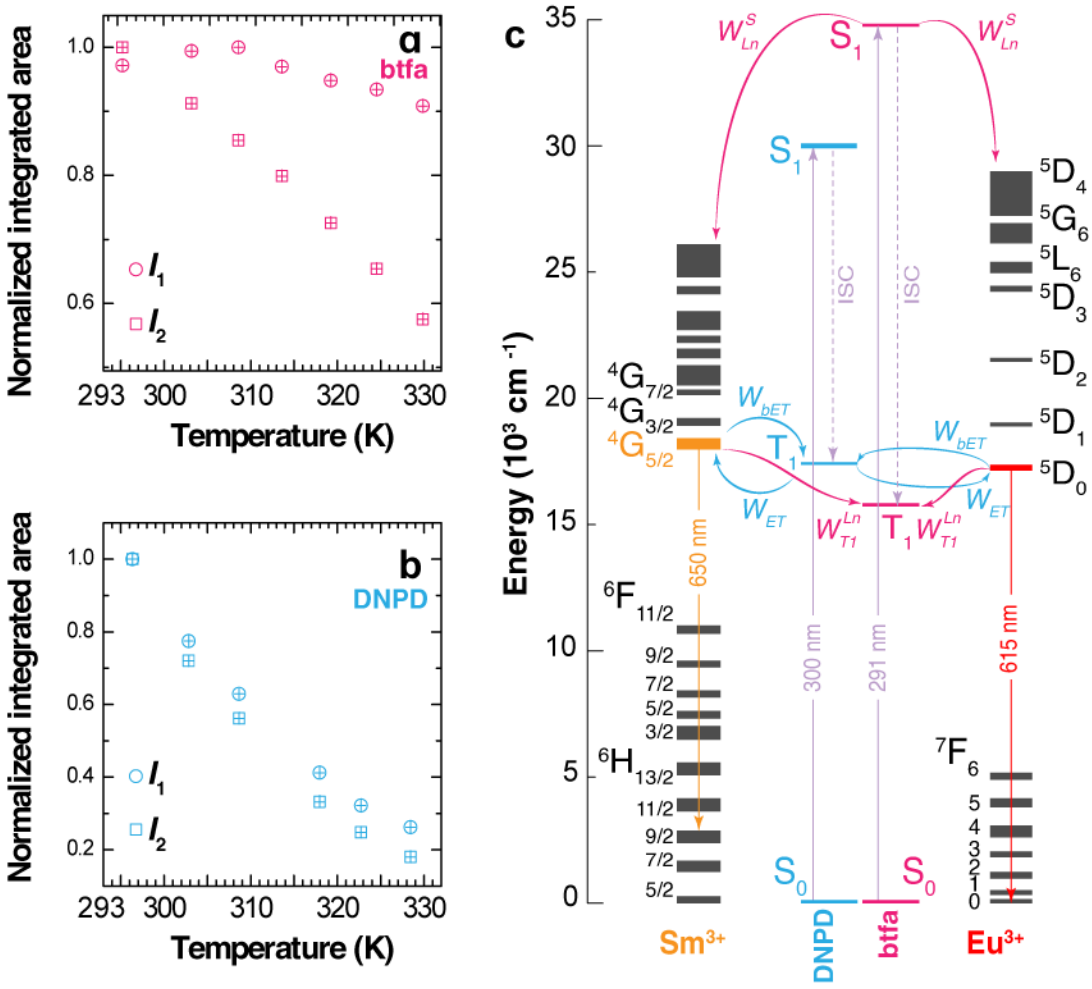

Figure 3. Temperature dependence of the integrated areas of the Sm^{3+} $^4G_{5/2}\rightarrow{}^6H_{9/2}$ (I_1) and the Eu^{3+} $^5D_0\rightarrow{}^7F_2$ (I_2) transitions in the Ln^{3+}-bearing **(a)** btfa- and **(b)** DNPD-based polymeric micelles. **(c)** Simplified energy level diagram for Sm^{3+}, Eu^{3+}, and ligands. The upwards arrow represents the initial absorptions by the ligands and ISC the intersystem crossing. For DNPD ligand, the forward intramolecular energy transfer rates (W_{ET}) are predominant via the $T_1\rightarrow{}^4G_{5/2}$ (Sm^{3+}) and $T_1\rightarrow{}^5D_0$ (Eu^{3+}) pathways. The backward energy transfer rates (W_{bET}) have a linear dependence with the temperature (Figure S6 in Supporting Information). For the btfa ligand, the forward intramolecular energy transfer rates ($\mathbf{W_{Ln}^S}$) occur essentially *via* the $S_1\rightarrow{}^4F_{5/2}$ (Sm^{3+}) and $S_1\rightarrow{}^5G_2$ (Eu^{3+}) pathways. In this case, the luminescence quenching depends on the energy balance between the transfer processes ($\mathbf{W}^*$), because the energy turns back to the ligand *via* the acceptor state T_1.

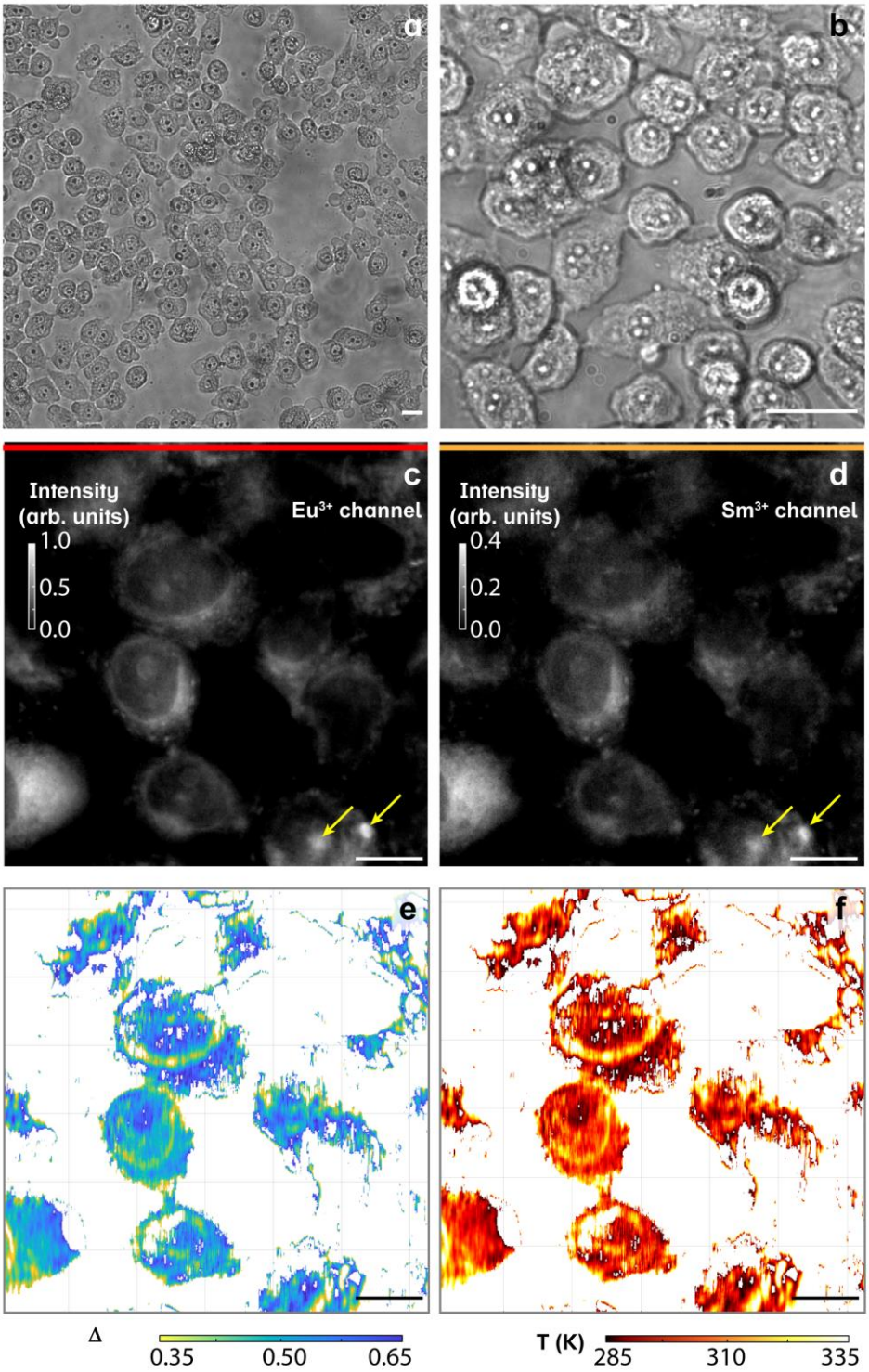

Figure 4. Room temperature microscopy images of MDA-MB-468 cells incubated with DNPD-based polymeric micelles under white-light illumination in **(a)** phase-contrast mode recorded with the color camera and **(b)** reflection mode recorded with the CMOS camera. Emission in the **(c)** Eu^{3+} and **(d)** Sm^{3+}channels recorded with the CMOS camera and illuminating the cultures with a 365 nm LED The yellow arrows sign illustrative brighter regions of the cells. Calculated 2D **(e)** Δ (using I_1 and I_2 channel images) and **(f)** temperature maps. All the scale bars correspond to 10 μm.

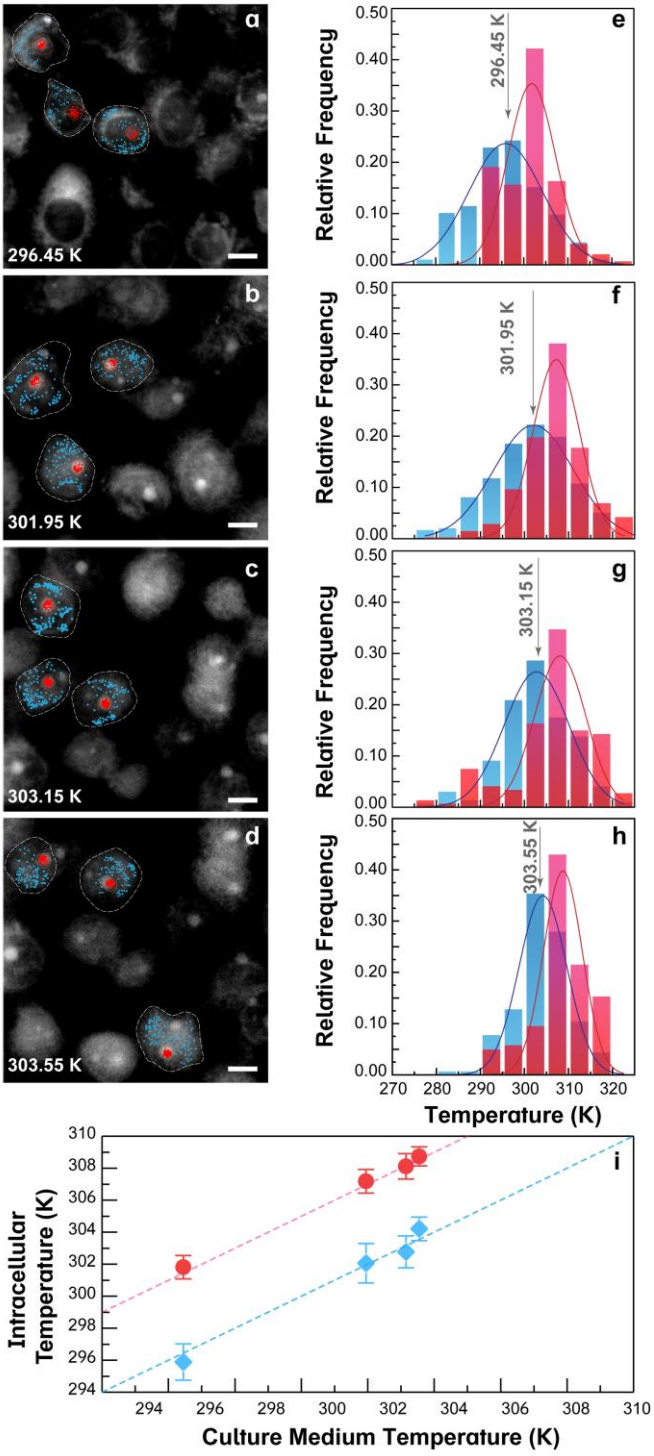

Figure 5. (a-d) Microscopy images (recorded in the Eu^{3+} channel) of the MDA-MB-468 cells incubated with DNPD-based polymeric micelles. The blue and red points mark, respectively, the locations used for temperature determination of the darker and brighter regions. The culture medium temperature values are indicated and The scale bars correspond to 10 μm. **(e-h)** Temperature histograms obtained from the selected points indicated in (a-d). The blue and red colors correspond to the blue (dark regions) and red (bright regions) points, respectively and the solid lines represent the best fits to Gaussian functions (r^2>0.90). **(i)** Temperature determined using the intracellular thermometer (y) versus culture medium temperature (x) for the dark (blue) and bright (red) regions (e-h histograms). The blue line corresponds to $y=x$ and the red one is shifted by 5 degrees (guides for the eyes).